Dependence of high-harmonic generation in twisted bilayer graphene on laser pulse ellipticity

M. S. Mrudul*

Department of Physics and Astronomy, P.O. Box 516, Uppsala University, S-75120 Uppsala, Sweden

(Received 9 May 2024; revised 19 August 2024; accepted 22 August 2024; published 10 September 2024)

The ellipticity of a laser pulse offers a control knob to tune the efficiency and polarization of emitted higher-order harmonics. In this paper, we systematically investigate the ellipticity dependence of high-harmonic generation in various bilayer graphene systems, such as AA-stacked, AB-stacked, and twisted bilayer graphene. We demonstrate how the underlying symmetries and electronic band structures of different bilayer systems distinctly contribute to the characteristics of ellipticity dependence, such as elliptical enhancement and elliptical dichroism. Additionally, we showcase a unique applicability of high-harmonic spectroscopy as a tool for identifying stacking faults in bilayer graphene systems. Our findings offer valuable insights into the nonlinear optical interactions of twisted bilayer graphene with different twist angles.

DOI: 10.1103/PhysRevB.110.115415

I. INTRODUCTION

The emergence of miniaturized quantum technologies traces back to the groundbreaking discovery of graphene [1]. Two-dimensional materials offer unprecedented advantages across various applications such as sensing, catalysis, energy storage, and the development of ultracompact electronic and optoelectronic devices [2–4]. One particularly fascinating aspect of two-dimensional materials is tunability, where techniques like strain engineering and doping can significantly modify their electronic properties [5–7]. Alternatively, manipulating the stacking configurations in multilayer two-dimensional systems brings novel physics, with van der Waals heterostructures as an example [8–10]. Recently, another intriguing stacking engineering approach was explored, involving the formation of a moiré pattern through the introduction of a relative twist between the layers in bilayer systems [11–13]. In particular, twisted bilayer graphene (TBG) around the magic angle near 1.1° exhibits fascinating physics, including unconventional superconductivity [12,14,15], correlated insulator behavior [11,15], emergent ferromagnetism [16], and a strange metal phase [17] to name but a few.

High-harmonic generation (HHG) is a strong-field frequency upconversion process [18], pioneered by Ghimire *et al.* in semiconductors [19]. In the past decade, high-harmonic spectroscopy has demonstrated its versatile potential in characterizing the electronic properties of bulk [20–46] and two-dimensional materials [47–58]. Specifically, high-harmonic spectroscopy of untwisted [59–61], and twisted bilayer graphene configurations was reported recently [62–64], revealing that the spectrum contains valuable insights about the underlying electronic structure and its symmetries. Moreover, recent studies in various multilayer two-dimensional materials revealed that the interlayer coupling has a significant role in the ultrafast electron dynamics [65–72].

It is known that controlling the polarization of the driving laser field allows one to tailor subcycle electron dynamics, which results in a desired control over polarization and the efficiency of emitted harmonics [30]. Moreover, distinct properties of a solid can be probed by optical response of different laser polarizations. Thus, ellipticity dependence of HHG provides critical insights regarding the electronic structure [30,45] as well as the underlying mechanism of HHG [25]. The ellipticity dependence in monolayer graphene has recently garnered significant interest due to the anomalous nature of the enhanced harmonic yield at a specific ellipticity [48]. Although the interesting ellipticity dependence in monolayer graphene has been explored in detail [60,73–75], a systematic comparison of the ellipticity dependence of HHG in different bilayer graphene systems, especially in TBG, is an unexplored territory.

The present paper focuses on a systematic and detailed investigation of the ellipticity dependence of HHG from different bilayer graphene configurations. We consider graphene bilayers with AA-stacked, AB-stacked, and twisted bilayer configurations. We find that the stacking order influences the ellipticity dependence significantly. The harmonic yield is optimal for a finite elipticity of the driving laser pulse. Moreover, symmetries arising from interlayer coupling in AB-stacked and TBG configurations play an important role in determining the characteristic ellipticity dependence. Furthermore, we demonstrate that the elliptical dichroism in HHG can serve as an all-optical characterization tool for stacking faults in bilayer graphene systems.

II. THEORETICAL METHODS

Graphene possesses a hexagonal unit cell with two nonequivalent carbon atoms, denoted as A and B. The lattice

*Contact author: mrudul.muraleedharan@physics.uu.se

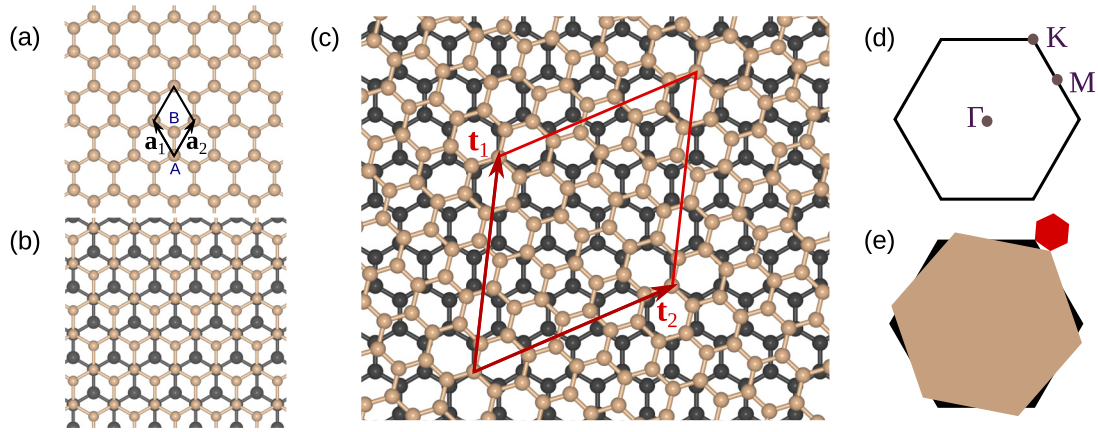

FIG. 1. Lattice structures of (a) AA-stacked, (b) AB-stacked, and (c) twisted bilayer graphene (TBG) systems. The twisted bilayer graphene in (c) has a twist of 13.17° between the layers. The red parallelogram represents the primitive unit cell of the TBG with lattice vectors $\mathbf{t}_1$ and $\mathbf{t}_2$. (d) The first Brillouin zone of the untwisted bilayer graphene. (e) The first Brillouin zones of the bottom (black) and top (brown) graphene layers, along with the resultant Brillouin zone of the TBG (red).

vectors of graphene are given by $\mathbf{a}_1 = a_0(-1/2,\sqrt{3}/2)$ and $\mathbf{a}_2 = a_0(1/2,\sqrt{3}/2)$ [see Fig. 1(a)]. A bilayer graphene can be formed by stacking graphene layers in the following configurations: (a) AA-stacked bilayer graphene, where the second layer is placed exactly on top of the first layer [Fig. 1(a)], (b) AB-stacked bilayer graphene (Bernel stacking), where A-type atoms in the top layer are positioned on top of B-type atoms in the bottom layer [Fig. 1(b)], and (c) TBG, characterized by a relative twist between the bottom and top layers, introducing a moiré pattern [Fig. 1(c)]. Among these configurations, AB-stacked graphene is the most energetically stable and commonly observed experimentally. Note that AB stacking can be seen as a special case of TBG, where the layers have a relative twist of 60°.

In this paper, we investigate TBG structures resulting from the commensurate rotation of the top layer relative to the bottom layer, following the methodology described in Refs. [76,77]. The TBG lattice vectors are defined as $\mathbf{t}_1 = n\mathbf{a}_1 + m\mathbf{a}_2$ and $\mathbf{t}_2 = -m\mathbf{a}_1 + (n+m)\mathbf{a}_2$ with n and m as integers. The primitive unit cell of TBG contains a total of $4(n^2 + m^2 + mn)$ atoms [76]. For instance, we obtain a TBG structure with a relative twist of 13.17° with 76 atoms in the unit cell for $(n, m) = (2, 3)$, as depicted in Fig. 1(c).

The tight-binding model focusing on the p_z orbitals of carbon atoms effectively describes the low-energy band structure of graphene [78]. The tight-binding Hamiltonian is given by

$$\mathcal{H}_{\mathbf{k}} = -\sum_{\mu\nu} \Upsilon_{\mu\nu} e^{i\mathbf{k}\cdot\mathbf{d}_{\mu\nu}} \hat{a}^{\dagger}_{\mu\mathbf{k}} \hat{a}_{\nu\mathbf{k}}. \tag{1}$$

Here, $\Upsilon_{\mu\nu}$ is the hopping integral between atomic sites μ and ν with position vectors $\mathbf{R}_\mu$ and $\mathbf{R}_\nu$. $\hat{a}^{\dagger}_{\mu\mathbf{k}}$ ($\hat{a}_{\mu\mathbf{k}}$) is the electron creation (annihilation) operator at the μth site. We define $\mathbf{d}_{\mu\nu} = \mathbf{R}_\mu - \mathbf{R}_\nu$, and $\Upsilon_{\mu\nu}$=$\Upsilon(\mathbf{d}_{\mu\nu})$. The hopping integral for bilayer graphene is parametrized as [77]

$$-\Upsilon(\mathbf{d}) = V_\pi(d)\left[1 - \left(\frac{\mathbf{d}\cdot\mathbf{e}_z}{d}\right)^2\right] + V_\sigma(d)\left(\frac{\mathbf{d}\cdot\mathbf{e}_z}{d}\right)^2, \tag{2}$$

where $d = |\mathbf{d}|$, and $\mathbf{e}_z$ is the unit vector along the out-of-plane direction. The intralayer hopping energy is $V_\pi(d) = V_\pi^0 e^{-(d-a)/\delta_0}$, and the interlayer hopping energy is $V_\sigma(d) = V_\sigma^0 e^{-(d-c)/\delta_0}$. Here, a is the interatomic distance, c is the interlayer separation, and δ_0 is the decay length. The lattice and tight binding parameters used are listed in Appendix A.

Let $\mathbf{A}$ denote the vector potential associated with its electric field $\mathbf{E}$, and they are related as $\mathbf{E} = -\partial\mathbf{A}/\partial t$. The time dependence in the Hamiltonian is introduced via the Peierls substitution within the dipole approximation as $\mathcal{H}_{\mathbf{k}}(t) = \mathcal{H}_{\mathbf{k}+\mathbf{A}(t)}$. We employ the density matrix formalism to describe laser-driven electron dynamics. The Liouville–von Neumann equation of motion [63] governing the density matrix operator at $\mathbf{k}$ is expressed as

$$\frac{d}{dt}\rho_{mn\mathbf{k}} = i[\hat{\rho}_{\mathbf{k}}, \hat{\mathcal{H}}_{\mathbf{k}+\mathbf{A}(t)}]_{mn} - \frac{(1-\delta_{mn})}{T_2}\rho_{mn\mathbf{k}}. \tag{3}$$

Equation (3) is solved by projecting the operators onto the eigenstates of the ground-state Hamiltonian in Eq. (1), $|n, \mathbf{k}\rangle$ ($\rho_{mn\mathbf{k}} = \langle m, \mathbf{k}|\hat{\rho}_{\mathbf{k}}|n, \mathbf{k}\rangle$). The last term on the right hand side accounts for electron-hole dephasing, where T_2 is the dephasing time and δ_{mn} is the Kronecker delta. We assume a dephasing time T_2 of 10 fs in the paper. The numerical integration is performed employing the fourth-order Runge-Kutta method with a time step of 0.02 fs.

The current operator at $\mathbf{k}$ is defined as

$$\hat{\mathbf{j}}_{\mathbf{k}} = \nabla_{\mathbf{k}}\mathcal{H}_{\mathbf{k}} = -i\sum_{\mu\nu} \mathbf{d}_{\mu\nu}\Upsilon_{\mu\nu} e^{i\mathbf{k}\cdot\mathbf{d}_{\mu\nu}} \hat{a}^{\dagger}_{\mu\mathbf{k}} \hat{a}_{\nu\mathbf{k}}. \tag{4}$$

Therefore, the laser-driven current within the density matrix formalism can be estimated as

$$\mathbf{j}(t) = \frac{1}{N_k}\sum_{\mathbf{k}} \mathrm{Tr}(\hat{\rho}_{\mathbf{k}}\,\hat{\mathbf{j}}_{\mathbf{k}+\mathbf{A}}). \tag{5}$$

Here, N_k is the number of k points. In the present paper, the reciprocal unit cell is sampled with a spacing of 0.014 Å^{-1}, while the length of the reciprocal lattice vector of graphene is 2.95 Å^{-1}.

The high-order harmonic spectrum is obtained by computing the Fourier transform of the time derivative of the current as [79]

$$\mathcal{I}(\omega) = \left| \mathcal{FT}\left(\frac{d}{dt}\mathbf{j}(t) \right) \right|^2. \tag{6}$$

The yield for the nth-order harmonic can be calculated using the formula $Y_{n\omega_0} = \int_{(n-\frac{1}{2})\omega_0}^{(n+\frac{1}{2})\omega_0} \mathcal{I}(\omega) d\omega$.

The vector potential associated with the laser pulse is defined as

$$\mathbf{A}(t) = \mathrm{Re}[\mathrm{A}_0 \mathbf{e}_p f(t) e^{i\omega_0 t}]. \tag{7}$$

Here, A_0 is the peak amplitude of the vector potential, ω_0 is the frequency of the laser pulse, $f(t)$ is a $\sin^2$ envelope function, and $\mathbf{e}_p$ is the polarization vector. The polarization vector of an elliptically polarized laser pulse with ellipticity ϵ and polarization angle θ can be written as $\mathbf{e}_p = \frac{1}{\sqrt{1+\epsilon^2}} \mathcal{R}_\theta \cdot (1, \mathrm{i}\epsilon)^T$, where $\mathcal{R}_\theta$ is the 2×2 rotation matrix. We employ laser pulses characterized by a peak intensity of 10^{11} W/cm^2, a wavelength of 3.2 μm (photon energy of 0.39 eV), and a duration of 85 fs. Throughout our paper, all laser parameters remain constant, except for the polarization properties denoted by ϵ and θ. The opposite signs of ϵ denote opposite helicity, where $\epsilon = \pm 1$ corresponds to circularly polarized laser fields, and $\epsilon = 0$ indicates a linearly polarized laser field. The results presented for AA-stacked and AB-stacked bilayer graphene configurations are performed in a supercell containing the same number of atoms as the TBG. We use the TBG configuration shown in Fig. 1(c) throughout the paper, unless stated otherwise.

III. RESULTS AND DISCUSSION

Figures 2(b)–2(d) present ellipticity dependence of HHG calculated for different bilayer graphene systems. The harmonic yields are normalized to the maximum harmonic yield, $Y_{n\omega_0}(\epsilon)/\max[Y_{n\omega_0}(\epsilon)]$. To ensure a fair comparison between different configurations, we align the major axis of the ellipse along the Γ-K direction in reciprocal space as shown in Fig. 2(a). The following interesting observations can be made.

(i) Symmetric harmonic yields, i.e., the yields of different harmonics, are insensitive to the incident laser helicity.

(ii) The ellipticity dependence demonstrates strong sensitivity to the stacking configuration of the bilayer graphene.

(iii) The peak harmonic yield occurs at a finite value of laser ellipticity.

Let us investigate how these peculiar features of the ellipticity dependence correlate with the underlying stacking configuration and the associated electronic structure.

A. Elliptical enhancement and stacking configuration

In atoms, the harmonic yield decays exponentially as the ellipticity of the driving laser increases. This behavior is explained by the semiclassical three-step model, where the recollision probability diminishes with increasing ellipticity [80,81]. However, elliptical enhancement is a characteristic feature of HHG from semiconductors [25,82]. This phenomenon highlights the existence of an optimal elliptical

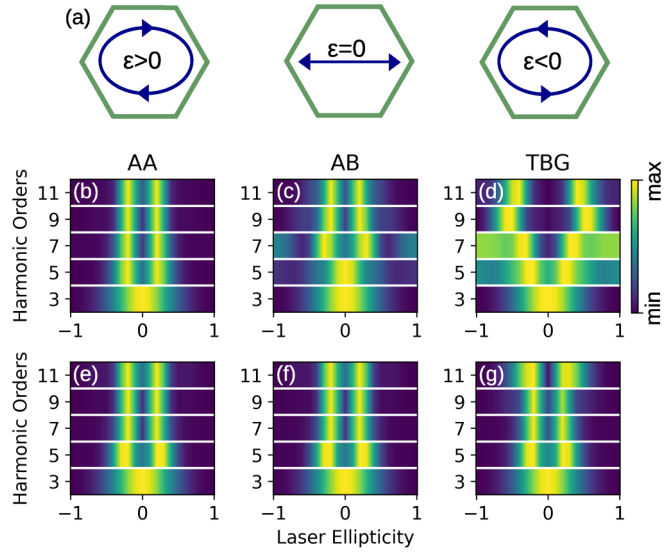

FIG. 2. Ellipticity dependence of the harmonic yield when the major axis of the ellipse is aligned along the Γ-K direction of the Brillouin zone, as shown in (a), for (b) AA-stacked, (c) AB-stacked, and (d) twisted bilayer graphenes. The harmonic yields are normalized to the peak yield of the corresponding harmonic order. Panels (e)–(g) show the same analysis as (b)–(d) without any interlayer coupling, i.e., $V_\sigma^0 = 0$.

polarization state that maximizes the efficiency of HHG in solids. Thus, understanding the mechanisms underlying the elliptical enhancement is crucial for optimizing the performance of nonlinear optical devices based on bilayer graphene. Previously, an anomalous elliptical enhancement has been experimentally observed in monolayer graphene [48]. Moreover, the elliptical enhancement in monolayer graphene, compared to AB-stacked bilayer graphene, was discussed in Ref. [60], which is consistent in the present case.

We follow Refs. [25,82] to understand the mechanism of elliptical enhancement. It is known that there are multiple optical paths that contribute to HHG in solids [20]: Exciting electrons between different energy bands contributes to interband polarization. Moreover, laser-excited electrons can be driven within the respective band, giving rise to intraband current. These competing mechanisms interfere constructively or destructively, depending on the energy and polarization of the emitted harmonic, resulting in a peculiar ellipticity dependence.

The band structures corresponding to different stacking configurations are compared in Appendix A [Figs. 9(a)–9(c)]. It is apparent that differences in band dispersions and interband dipole matrix elements lead to distinct interband and intraband contributions to harmonic emission. The interband electron dynamics is governed by the coupling term $\mathbf{e}_p \cdot \mathbf{p}_{mn}$, where $\mathbf{p}_{mn}$ is the momentum matrix element between mth and nth energy bands. So, the polarization vector of the laser field, $\mathbf{e}_p$, also has a strong role in determining the ultrafast electron dynamics. The band structures of the AA- and AB-stacked bilayer graphene configurations consist of four bands in the primitive unit cell [60]. Consequently, electrons in the valence bands have a maximum of two interband

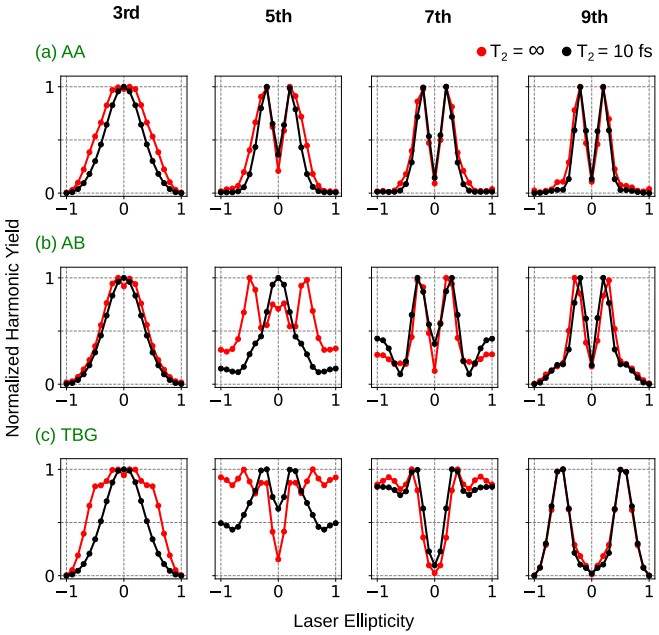

FIG. 3. Ellipticity dependence of the harmonic yield for finite (black, $T_2 = 10$ fs) and infinite (red) dephasing time in (a) AA-stacked, (b) AB-stacked, and (c) TBG configurations. All harmonic yields are normalized to the peak yield.

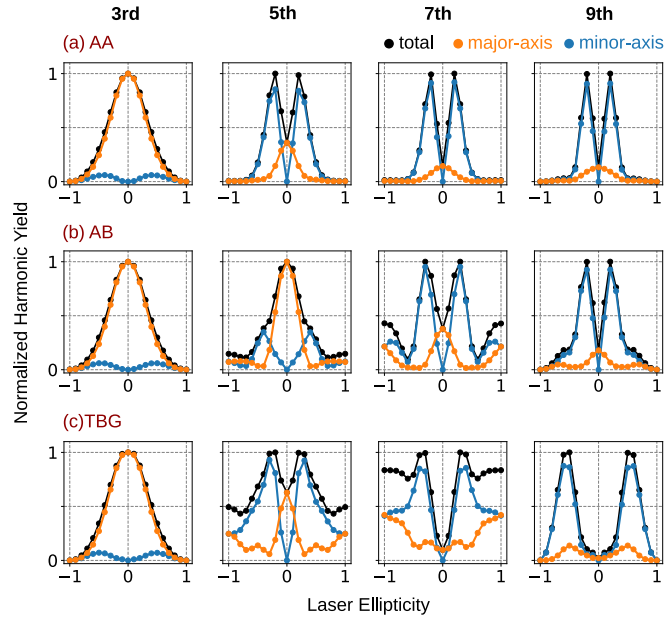

FIG. 4. Direction-resolved contributions to the ellipticity dependence in (a) AA-stacked, (b) AB-stacked, and (c) TBG configurations. Harmonic yields are resolved along the major (orange) and the minor (blue) axis of the polarization ellipse. All harmonic yields are normalized to the peak of the total yield (black).

channels for excitations. Conversely, the band structure of the TBG with N_{at} atoms comprises $N_{at}/2$ valence and $N_{at}/2$ conduction bands when calculated in the primitive unit cell. Therefore, each electron in the valence band has $N_{at}/2$ interband channels to the conduction bands. These additional interband channels in TBG give rise to its peculiar ellipticity dependence and result in much pronounced elliptical enhancement compared to AA-stacked and AB-stacked bilayers (see Fig. 10). In short, nonlinear processes and their dynamic interference are considerably different in different bilayer graphene configurations, resulting in the stacking-sensitive ellipticity dependence, as shown in Figs. 2(b)–2(d). Furthermore, the intraband contribution dominates near the Fermi energy, primarily due to the limited joint density of states for the interband transitions [60]. Consequently, the elliptical enhancement is weak for the third-order harmonic. Note that a correlation between the band structure and HHG from TBG has been established, which can be utilized to characterize the magic angle of the TBG [64].

We further investigate the significance of electron-hole dephasing on the observed ellipticity dependence. Figure 3 compares the ellipticity dependence of harmonic yield with and without accounting for dephasing. It is noteworthy that the presence of dephasing significantly alters the harmonic yields, particularly for the fifth harmonic in AB-stacked bilayer graphene and the fifth and seventh harmonics in TBG. This underscores the importance of including appropriate dephasing channels in modeling high-order harmonic processes.

Let us turn our discussion to the role of interlayer coupling in the ellipticity dependence as shown in Figs. 2(e)–2(g). We consider two graphene layers arranged as in Figs. 1(a)–1(c) without any interlayer coupling, i.e., $V_\sigma^0 = 0$. The results in Figs. 2(e) and 2(f) are identical to that of monolayer graphene, while Fig. 2(g) is for two layers of graphene in a twisted configuration. It is interesting to note that the ellipticity dependence of the AA-stacked bilayer graphene [Fig. 2(b)] resembles that of monolayer graphene [Fig. 2(e)]. This is in agreement with previous work on monolayer and AA-stacked bilayer graphene exposed to a linearly polarized laser field [60]. It was attributed to the comparable interband matrix elements resulting from the same point group symmetry of these materials [60]. On the other hand, interlayer coupling strongly modifies the harmonic emission in AB-stacked and TBG configurations. In TBG, we observe differences in the ellipticity dependence compared to that of monolayer graphene, even without interlayer coupling as evident from Fig. 2(g). This is because the polarization vector of the laser field is aligned along different symmetry directions for the top and bottom graphene layers [63]. Thus, the interference of currents from different layers creates a distinct ellipticity dependence compared to monolayer graphene. Therefore, the arrangement of atoms in TBG is also an important factor determining its characteristic ellipticity dependence.

We further explore the direction-resolved contribution to the ellipticity dependence in Figs. 4(a)–4(c). The harmonic yields are calculated for the current components along the major and minor axis to the polarization ellipse. Interestingly, for all the bilayer graphene configurations, the peak harmonic yield at finite ellipticity (for harmonics higher than third) is dominantly polarized along the minor axis of the ellipse. This is in agreement with the experimentally observed anomalous ellipticity dependence for monolayer graphene [48]. The intensity of the laser field along the major axis of the po-

larization ellipse (I^{major}) is proportional to $1/(1+\epsilon^2)$ and the intensity along the minor axis (I^{minor}) is proportional to $\epsilon^2/(1+\epsilon^2)$. Therefore, the ratio of these intensities is $I^{\text{minor}}/I^{\text{major}} = \epsilon^2$. It is apparent that the generated harmonics do not follow this trend. This peculiar ellipticity dependence shows how the polarization states of the emitted harmonics drastically differ from the polarization of the laser field. However, for linearly ($\epsilon = 0$) and circularly ($|\epsilon| = 1$) polarized laser fields, the emitted harmonics show characteristics similar to the laser field, with $Y^{\text{minor}}_{n\omega_0}/Y^{\text{major}}_{n\omega_0} \approx \epsilon^2$.

The ellipticity dependence for other TBG configurations is presented in Appendix C. The preceding conclusions can be applied to TBG configurations of different twist angles. Additionally, we observe a significant enhancement of circularly polarized ($|\epsilon| = 1$) fifth and seventh harmonics in all TBG configurations studied [Figs. 11(a)–11(c)]. In short, the stacking modifications through interlayer twist can be utilized to optimize the efficiency and polarization of higher-order harmonics. So far, we have focused on the ellipticity dependence of laser pulses, specifically when their major axis aligns with the Γ-K direction of the Brillouin zone. In the following, we will explore the symmetries of harmonic yield as a function of the polarization axis of the laser field.

B. Anisotropic ellipticity dependence and elliptical dichroism

In contrast to the circularly polarized laser, the elliptically polarized laser offers an additional in-plane degree of freedom beyond helicity, i.e., polarization direction. The relative orientation of the sample and the laser polarization can be controlled through the polarization rotation, denoted as θ [see the definition of $\mathbf{e}_p$ following Eq. (7)]. Figures 5(a)–5(c) demonstrate the anisotropic modulation of harmonic yields as a function of the laser's polarization for different bilayer stacking configurations. Here, the laser ellipticity is held constant at ± 0.3, and θ is defined relative to the Γ-K direction in the Brillouin zone. Note that the following observations and their physical interpretations hold true for other values of ϵ.

The polarization angle dependence on harmonic yields depicted in Fig. 5 is strongly sensitive to the stacking configuration, similar to the ellipticity dependence observed in Fig. 2. Remarkably, we observe a phenomenon known as elliptical dichroism, where the harmonic yield differs for opposite helicities of the laser pulse, i.e., $Y_{n\omega_0}(\epsilon) \neq Y_{n\omega_0}(-\epsilon)$. The elliptical dichroism is less pronounced for AA-stacked bilayer graphene [Fig. 5(a)] in comparison to AB-stacked [Fig. 5(b)] and TBG configurations [Fig. 5(c)]. Moreover, the anisotropic elliptical dichroism exhibits the symmetry pattern $Y_{n\omega_0}(\epsilon, \theta) = Y_{n\omega_0}(-\epsilon, -\theta)$, where θ can be defined with respect to either of the high-symmetry directions (Γ-K or Γ-M). As a special case, the harmonic yield is unaffected by the helicity of the laser pulse when the major axis of the ellipse is aligned along Γ-K (also shown in Fig. 2) and Γ-M.

Next, we explore how the observed elliptical dichroism is linked to the symmetries of the bilayer graphene and the laser pulse. Figures 6(a)–6(c) show the relevant symmetries of the bilayer graphene configurations with respect to the Γ-K direction of the Brillouin zone (red dashed lines). All bilayer graphene configurations possess a twofold rotational axis (C_2) that passes through the layers [62]. Additionally,

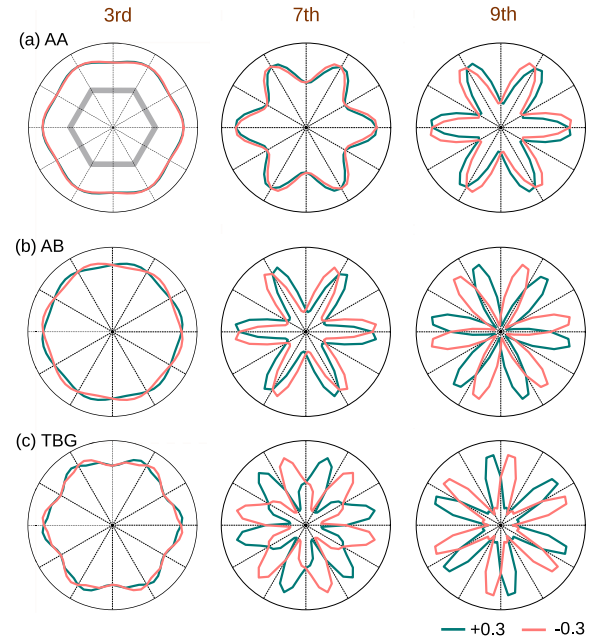

FIG. 5. Polarization-direction dependence of harmonic yields for (a) AA-stacked, (b) AB-stacked, and (c) TBG configurations. The green (pink) lines represent harmonic yields for an elliptically polarized driver with an ellipticity of $+0.3$ (-0.3). The angle of polarization, θ, is defined with respect to the Γ-K direction of the Brillouin zone.

AA-stacked bilayer graphene has a vertical reflection plane (σ_v), as illustrated in Fig. 6(a).

Let us examine the dynamical symmetries related to an elliptically polarized laser interacting with the bilayer graphene. We begin by considering a case where the major axis of the

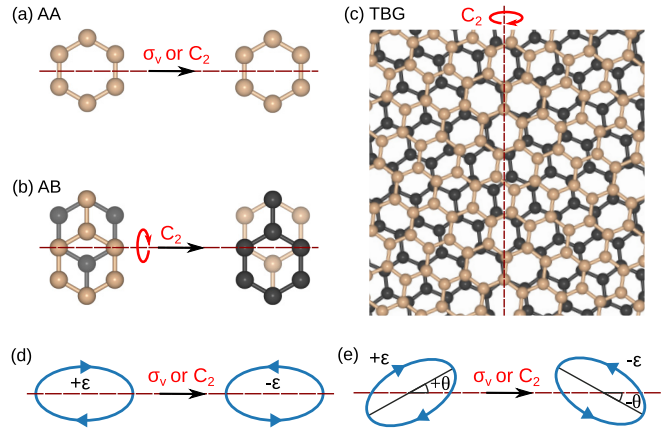

FIG. 6. Spatial symmetries associated with (a) AA-stacked, (b) AB-stacked, and (c) TBG configurations. Symmetry transformations of the Lissajous profile of the vector potential when the laser field has its major axis (d) along the Γ-K direction of the Brillouin zone, and (e) rotated by the polarization angle θ. Red dashed lines indicate the Γ-K direction of the Brillouin zone. σ_v indicates the vertical symmetry plane, and C_2 is the axis of twofold rotational symmetry.

laser field is aligned along the Γ-K direction of the Brillouin zone. The Lissajous profile illustrating this scenario is presented in Fig. 6(d). In this case, applying a σ_v or C_2 operation to the Lissajous profile reverses the helicity of the laser field. In other words, reversing the helicity of the laser field is equivalent to applying the σ_v or C_2 symmetry on the lattice. Since bilayer graphenes are invariant under these symmetry operations [Figs. 6(a)–6(c)], harmonic yields corresponding to the opposite helicities remain identical as shown in Fig. 2.

Now, we generalize the symmetry arguments when the major axis of the elliptical laser field is rotated with a polarization angle θ. The scenario is depicted in Fig. 6(e). Here, applying the spatial symmetry σ_v or C_2 on the lattice is equivalent to transforming the polarization state of the laser field as $(\epsilon, \theta) \rightarrow (-\epsilon, -\theta)$. Thus, the dynamical symmetry dictates the observed symmetries of the harmonic yield as $Y_{n\omega_0}(\epsilon, \theta) = Y_{n\omega_0}(-\epsilon, -\theta)$ [45]. Note that Γ-K and Γ-M are perpendicular symmetry directions for a hexagonal lattice. Thus, when the major axis of the ellipse aligns along the Γ-K direction, the minor axis aligns with the Γ-M direction and vice versa. Therefore, the same dynamical symmetry arguments can be translated to explain the absence of elliptical dichroism when the major axis of the ellipse is along the Γ-M direction.

Note that in Ref. [41], the authors proposed that elliptical dichroism of harmonics can be used as a probe to identify the topological phase, which was recently debated in Ref. [45]. So, it is essential to understand what are the symmetries responsible for the elliptical dichroism in HHG. Finally, it is important to remark that the dynamical symmetries presented above do not provide a quantitative description of the elliptical dichroism. The extent of elliptical dichroism strongly depends on the interlayer coupling, band structure, and underlying symmetries.

C. Layer-resolved contributions

In this section, we delve into the layer-resolved contributions to the ellipticity dependence of HHG. The layer-resolved contributions to the current can be estimated using the operator,

$$\hat{\mathbf{j}}_{l,\mathbf{k}} = -i \sum_{\mu,\nu \in l} \mathbf{d}_{\mu\nu} \Upsilon_{\mu\nu} e^{i\mathbf{k}\cdot\mathbf{d}_{\mu\nu}} \hat{a}^{\dagger}_{\mu,\mathbf{k}} \hat{a}_{\nu,\mathbf{k}}, \tag{8}$$

where the summation is restricted to the atomic sites in the lth graphene layer [62,63]. The total current comprises the intralayer contribution as defined above and interlayer contribution where hopping between atomic sites of different layers is considered [see Eq. (4)].

Figures 7(a)–7(c) illustrate the layer-resolved high-harmonic ellipticity dependence for different bilayer graphene configurations. The major axis of the ellipse is aligned along the Γ-K direction of the Brillouin zone, consistent with Fig. 2. We observe that the total harmonic yields (black lines) are dominated by intralayer contributions (blue lines). Interestingly, the top and bottom layers contribute identically to the harmonic yield for AA-stacked bilayer graphene [Fig. 7(a)]. In contrast, the harmonic yields differ for the top and bottom layers in AB-stacked [Fig. 7(b)] and TBG [Fig. 7(c)] configurations.

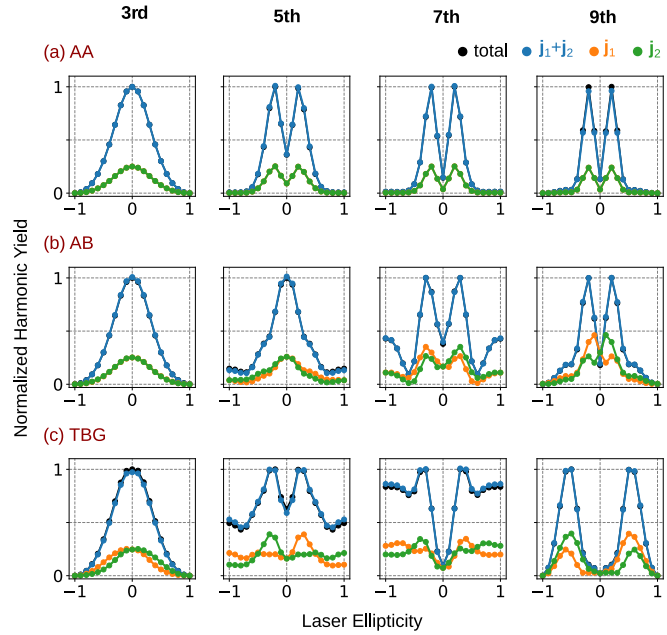

FIG. 7. Layer-resolved contributions to the ellipticity dependence of HHG in (a) AA-stacked, (b) AB-stacked, and (c) TBG configurations. Harmonic yields are normalized to the peak yield estimated from the total current $\mathbf{j}$ (black). Orange and green lines denote harmonic yields estimated from the current generated in the bottom ($\mathbf{j}_1$) and top ($\mathbf{j}_2$) layers, respectively.

Next, we analyze the symmetries associated with the layer-resolved ellipticity dependence for AB-stacked and twisted bilayer graphene configurations. Let the nth harmonic yield calculated for the lth graphene layer be defined as $Y^l_{n\omega_0}(\epsilon)$. The harmonic yields from each layer exhibit elliptical dichroism, where $Y^l_{n\omega_0}(-\epsilon) \neq Y^l_{n\omega_0}(\epsilon)$. Concisely, the harmonic yields of the top and bottom layers under the flip of helicity are related as $Y^1_{n\omega_0}(-\epsilon) = Y^2_{n\omega_0}(\epsilon)$. In monolayer graphene, the distinct A and B carbon atoms are related by the reflection symmetry, σ_v [see Fig. 1(a)]. This symmetry governs the excitation under opposite elliptical helicity, resulting in symmetric harmonic yields in graphene [Fig. 2(e)]. Notably, in AA-stacked bilayer graphene, the in-plane symmetry between A and B atoms is preserved [Fig. 6(a)]. Consequently, electrons in the top and bottom graphene layers are excited identically under an elliptically polarized driver, as shown in Fig. 7(a).

On the other hand, in AB-stacked bilayer graphene, the reflection symmetry connecting A and B atoms within the layer is broken due to the interlayer coupling [Fig. 6(b)]. The absence of the in-plane symmetry results in elliptical dichroism of the layer-resolved harmonic yield. In addition, the C_2 symmetry exchanges top and bottom layers, resulting in the characteristic relation observed in Fig. 7(b). The same explanation of AB-stacked bilayer graphene is applicable for the TBG, where the σ_v plane is absent, and the C_2 axis is present [Fig. 7(c)].

D. Stacking fault and elliptical dichroism

Up to this point, we have established how the stacking configurations of bilayer graphene result in its different ellipticity

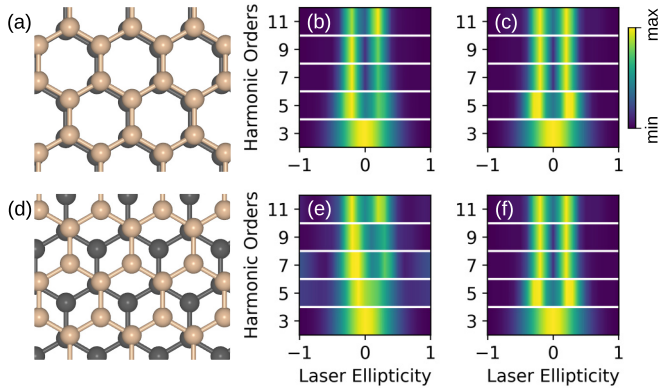

FIG. 8. The high-harmonic ellipticity dependence in panels (b) and (e) corresponds to distorted bilayer graphene configurations shown in panels (a) and (d), respectively. Panels (c) and (f) present the same analysis as (b) and (e), respectively, but without interlayer coupling. The yield of each harmonic is normalized to the peak yield.

dependence. Moreover, the layer-resolved harmonic yields are mutually related for opposite laser helicities in AB-stacked and twisted bilayer graphene configurations. This leads us to the natural question: How effective is this method in identifying stacking faults in bilayer systems? This section explores the elliptical dichroism resulting from stacking faults in the bilayer graphene.

Figures 8(a) and 8(d) show two bilayer configurations with stacking misalignment, created by a relative displacement between the layers of AA-stacked [Fig. 8(a)] and AB-stacked [Fig. 8(d)] bilayer graphene. Here, all atoms in the top graphene layer are displaced by the vector $\mathbf{\Delta} = \Delta_0(1, 1, 0)$, where $\Delta_0 = 0.14$Å. Note that this change does not affect the periodicity or the lattice vectors (or reciprocal lattice vectors) of the material. Thus, the Brillouin zone of the misaligned bilayer remains the same as that of the pristine bilayer. We refer to the structure in Fig. 8(a) as m-AA and the structure in Fig. 8(d) as m-AB.

Figures 8(b) and 8(e) present the ellipticity dependence for m-AA and m-AB bilayer graphene configurations, respectively. The major axis of the ellipse aligns along the Γ-K direction of the Brillouin zone, consistent with Fig. 2. We observe strong elliptical dichroism for harmonic orders higher than third, with the effect being more prominent for the m-AB structure. The elliptical dichroism arises due to the absence of σ_v or C_2 symmetry in the misaligned bilayer graphene configurations. It is noteworthy that even a minor stacking mismatch results in a significant elliptical dichroism. The elliptical dichroism in higher-order harmonics due to stacking faults in different TBG configurations is presented in Fig. 12.

Figures 8(c) and 8(f) show the ellipticity dependence in the absence of interlayer coupling for m-AA and m-AB configurations, respectively. As the intralayer symmetries are not broken and Γ-K is still a high-symmetry direction for the individual layers, there is no elliptical dichroism in this case. Thus, the harmonic ellipticity dependences in Figs. 8(c) and 8(f) are identical to that of monolayer graphene.

Thus, the ellipticity dependence is a powerful tool in exploring the stacking configurations and stacking faults in bilayer graphene systems. It is important to mention that Raman spectroscopy is another robust all-optical technique that characterizes graphene and graphene-derivative structures [83,84]. In particular, Raman spectroscopy can characterize the stacking configurations by probing the out-of-plane vibrations [85]. On the other hand, we demonstrated here that the high-harmonic spectroscopy strongly depends on the interlayer coupling and the resultant symmetries. So, high-harmonic spectroscopy can be used as a complementary technique that can probe interlayer phonon modes with subfemtosecond temporal resolution [86–88].

IV. SUMMARY

In summary, we studied the ellipticity dependence of high-harmonic generation in various bilayer graphene configurations such as AA-stacked, AB-stacked, and TBG. We demonstrated that different bilayer graphene structures show anomalous elliptical enhancement in the higher-order harmonics. The ellipticity dependence is strongly anisotropic and exhibits elliptical dichroism when the major axis of the ellipse aligns along a direction other than high symmetry directions. Moreover, we demonstrated that the elliptical dichroism is related to the spatial symmetries of the bilayer graphene. Further, the elliptical enhancement and dichroism in different bilayer graphene configurations are strongly sensitive to the stacking configuration and the electronic band structure. In addition, we demonstrated that a slight stacking fault results in pronounced elliptical dichroism in the bilayer graphene. Thus, ellipticity dependence can be used as a potential characterization technique to probe numerous bilayer graphene configurations. Moreover, we propose high-harmonic ellipticity dependence as a complementary technique that has potential to probe coherent interlayer phonon modes with subfemtosecond temporal resolution.

ACKNOWLEDGMENTS

We acknowledge fruitful discussion with P. M. Oppeneer (Uppsala University), G. Dixit (IIT Bombay), M. Weißenhofer (Uppsala University), and D. Chakraborty (MPIPKS, Dresden). This work has been supported by the K. and A. Wallenberg Foundation (Grants No. 2022.0079 and No. 2023.0336). The calculations were enabled by resources provided by the National Academic Infrastructure for Supercomputing in Sweden funded by the Swedish Research Council through Grant No. 2022-06725.

APPENDIX A: ELECTRONIC BAND STRUCTURES

The lattice and tight-binding parameters are adapted from Ref. [77]. The nearest-neighbor distance, a, is 1.42 Å, with a lattice parameter of $a_0 = 2.46$ Å, and an interlayer separation $c = 3.35$ Å. The intralayer and interlayer coupling strengths are $V_\pi^0 = -2.7$ eV and $V_\sigma^0 = 0.48$ eV, respectively. The decay length of the hopping integral is approximately $0.184a_0$, chosen to match the dispersion of AB-stacked bilayer graphene. All hopping within the limit $d < 4a$ is considered. We use the

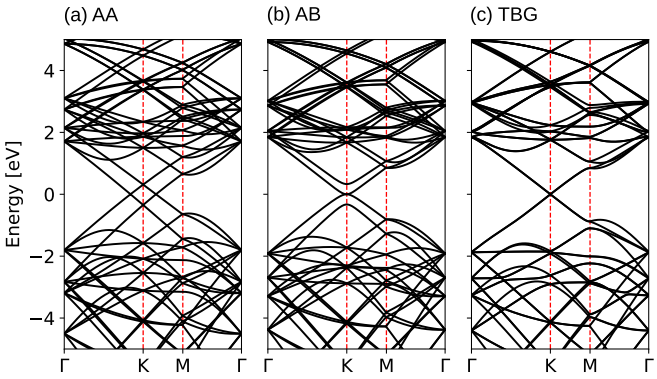

FIG. 9. Electronic band structures for (a) AA-stacked, (b) AB-stacked, and (c) TBG configurations. Here, TBG with a twist angle of 13.17°, as depicted in Fig. 1(c), is considered.

same hopping parameters for different stacking configurations shown in Figs. 1(a)–1(c). The band structures for different stacking configurations are compared in Figs. 9(a)–9(c). Note that that the bands for AA-stacked and AB-stacked bilayer graphene are calculated in the supercell with the same number of atoms as TBG.

APPENDIX B: HHG SPECTRUM

HHG spectrum for AA stacked, AB stacked, and TBG configurations are compared in Fig. 10. The results for linearly polarized pulse ($\epsilon = 0$) and elliptically polarized pulse ($\epsilon = 0.3$) are shown respectively in Figs. 10(a) and 10(b).

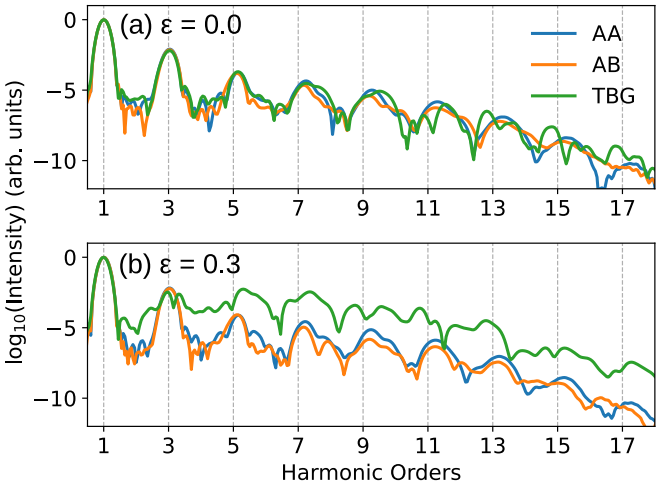

FIG. 10. HHG spectrum for AA-stacked (blue), AB-stacked (orange), and TBG (green) configurations for a laser with ellipticity (a) $\epsilon = 0.0$ and (b) $\epsilon = 0.3$. Here, TBG with a twist angle of 13.17°, as depicted in Fig. 1(c), is considered. The laser parameters are the same as in Fig. 2.

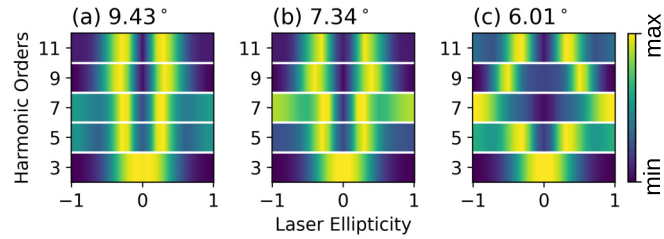

FIG. 11. Ellipticity dependence of TBG with twist angles of (a) 9.43°, (b) 7.34°, and (c) 6.01°. The yield of each harmonic is normalized to the maximum yield.

APPENDIX C: ELLIPTICITY DEPENDENCE FOR OTHER TWIST ANGLES

The high-harmonic ellipticity dependences for TBG with different twist angles are presented in Figs. 11(a)–11(c). Figure 11(a) corresponds to a twist angle of 9.43° [$(n, m) = (3, 4)$], with 148 atoms in the unit cell. Figure 11(b) corresponds to a twist angle of 7.34° [$(n, m) = (4, 5)$], with 244 atoms in the unit cell. Figure 11(c) corresponds to a twist angle of 6.01° [$(n, m) = (5, 6)$], with 364 atoms in the unit cell.

APPENDIX D: PROBING STACKING FAULTS IN TBG

The high-harmonic ellipticity dependences for TBG of different twist angles with stacking faults are presented in Figs. 12(a)–12(d). The misalignment between the layers of TBG is created by displacing the top graphene layer by the vector $\mathbf{\Delta}$.

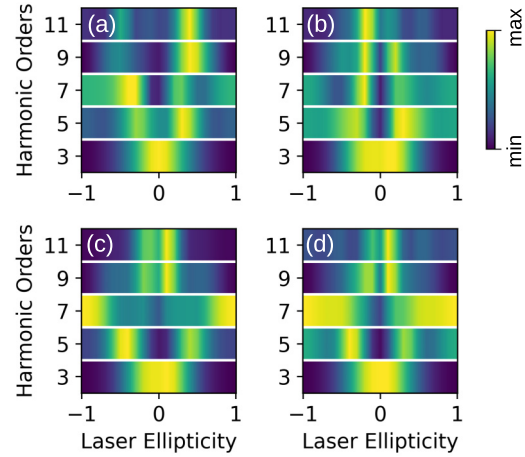

FIG. 12. Ellipticity dependence of the harmonic yield for distorted TBG with twist angles of (a) 13.17°, (b) 9.43°, (c) 7.34°, and (d) 6.01°. The yield of each harmonic is normalized to the peak yield.

[1] K. S. Novoselov, A. K. Geim, S. V. Morozov, D.-E. Jiang, Y. Zhang, S. V. Dubonos, I. V. Grigorieva, and A. A. Firsov, Electric field effect in atomically thin carbon films, Science **306**, 666 (2004).

[2] A. K. Geim and K. S. Novoselov, The rise of graphene, Nat. Mater. **6**, 183 (2007).

[3] D. Jariwala, V. K. Sangwan, L. J. Lauhon, T. J. Marks, and M. C. Hersam, Emerging device applications for semiconducting two-dimensional transition metal dichalcogenides, ACS Nano **8**, 1102 (2014).

[4] C. Liu, H. Chen, S. Wang, Q. Liu, Y.-G. Jiang, D. W. Zhang, M. Liu, and P. Zhou, Two-dimensional materials for next-generation computing technologies, Nat. Nanotechnol. **15**, 545 (2020).

[5] R. Roldán, A. Castellanos-Gomez, E. Cappelluti, and F. Guinea, Strain engineering in semiconducting two-dimensional crystals, J. Phys.: Condens. Matter **27**, 313201 (2015).

[6] G. Fiori, F. Bonaccorso, G. Iannaccone, T. Palacios, D. Neumaier, A. Seabaugh, S. K. Banerjee, and L. Colombo, Electronics based on two-dimensional materials, Nat. Nanotechnol. **9**, 768 (2014).

[7] H. Wang, H. Yuan, S. S. Hong, Y. Li, and Y. Cui, Physical and chemical tuning of two-dimensional transition metal dichalcogenides, Chem. Soc. Rev. **44**, 2664 (2015).

[8] A. K. Geim and I. V. Grigorieva, Van der Waals heterostructures, Nature (London) **499**, 419 (2013).

[9] Y. Liu, N. O. Weiss, X. Duan, H.-C. Cheng, Y. Huang, and X. Duan, Van der Waals heterostructures and devices, Nat. Rev. Mater. **1**, 16042 (2016).

[10] K. S. Novoselov, A. Mishchenko, A. Carvalho, and A. H. Castro Neto, 2D materials and van der Waals heterostructures, Science **353**, aac9439 (2016).

[11] Y. Cao, V. Fatemi, A. Demir, S. Fang, S. L. Tomarken, J. Y. Luo, J. D. Sanchez-Yamagishi, K. Watanabe, T. Taniguchi, E. Kaxiras *et al.*, Correlated insulator behaviour at half-filling in magic-angle graphene superlattices, Nature (London) **556**, 80 (2018).

[12] Y. Cao, V. Fatemi, S. Fang, K. Watanabe, T. Taniguchi, E. Kaxiras, and P. Jarillo-Herrero, Unconventional superconductivity in magic-angle graphene superlattices, Nature (London) **556**, 43 (2018).

[13] E. Y. Andrei and A. H. MacDonald, Graphene bilayers with a twist, Nat. Mater. **19**, 1265 (2020).

[14] M. Yankowitz, S. Chen, H. Polshyn, Y. Zhang, K Watanabe, T Taniguchi, D. Graf, A. F. Young, and C. R. Dean, Tuning superconductivity in twisted bilayer graphene, Science **363**, 1059 (2019).

[15] X. Lu, P. Stepanov, W. Yang, M. Xie, M. A. Aamir, I. Das, C. Urgell, K. Watanabe, T. Taniguchi, G. Zhang *et al.*, Superconductors, orbital magnets and correlated states in magic-angle bilayer graphene, Nature (London) **574**, 653 (2019).

[16] A. L. Sharpe, E. J. Fox, A. W. Barnard, J. Finney, K. Watanabe, T. Taniguchi, M. A. Kastner, and D. Goldhaber-Gordon, Emergent ferromagnetism near three-quarters filling in twisted bilayer graphene, Science **365**, 605 (2019).

[17] Y. Cao, D. Chowdhury, D. Rodan-Legrain, O. Rubies-Bigorda, K. Watanabe, T. Taniguchi, T Senthil, and P. Jarillo-Herrero, Strange metal in magic-angle graphene with near planckian dissipation, Phys. Rev. Lett. **124**, 076801 (2020).

[18] M. Ferray, A. L'Huillier, X. F. Li, L. A. Lompre, G. Mainfray, and C. Manus, Multiple-harmonic conversion of 1064 nm radiation in rare gases, J. Phys. B **21**, L31 (1988).

[19] S. Ghimire, A. D. DiChiara, E. Sistrunk, P. Agostini, L. F. DiMauro, and D. A. Reis, Observation of high-order harmonic generation in a bulk crystal, Nat. Phys. **7**, 138 (2011).

[20] G. Vampa, C. R. McDonald, G. Orlando, D. D. Klug, P. B. Corkum, and T. Brabec, Theoretical analysis of high-harmonic generation in solids, Phys. Rev. Lett. **113**, 073901 (2014).

[21] G. Vampa, T. J. Hammond, N. Thiré, B. E. Schmidt, F. Légaré, C. R. McDonald, T. Brabec, and P. B. Corkum, Linking high harmonics from gases and solids, Nature (London) **522**, 462 (2015).

[22] T. T. Luu, M. Garg, S. Yu. Kruchinin, A. Moulet, M. Th. Hassan, and E. Goulielmakis, Extreme ultraviolet high-harmonic spectroscopy of solids, Nature (London) **521**, 498 (2015).

[23] M. Hohenleutner, F. Langer, O. Schubert, M. Knorr, U. Huttner, S. W. Koch, M. Kira, and R. Huber, Real-time observation of interfering crystal electrons in high-harmonic generation, Nature (London) **523**, 572 (2015).

[24] N. Tancogne-Dejean, O. D. Mücke, F. X. Kärtner, and A. Rubio, Impact of the electronic band structure in high-harmonic generation spectra of solids, Phys. Rev. Lett. **118**, 087403 (2017).

[25] N. Tancogne-Dejean, O. D. Mücke, F. X. Kärtner, and A. Rubio, Ellipticity dependence of high-harmonic generation in solids originating from coupled intraband and interband dynamics, Nat. Commun. **8**, 745 (2017).

[26] R. E. F. Silva, I. V. Blinov, A. N. Rubtsov, O. Smirnova, and M. Ivanov, High-harmonic spectroscopy of ultrafast many-body dynamics in strongly correlated systems, Nat. Photonics **12**, 266 (2018).

[27] I. Floss, C. Lemell, G. Wachter, V. Smejkal, S. A. Sato, X. M. Tong, K. Yabana, and J. Burgdörfer, *Ab initio* multiscale simulation of high-order harmonic generation in solids, Phys. Rev. A **97**, 011401(R) (2018).

[28] F. Langer, C. P. Schmid, S. Schlauderer, M. Gmitra, J. Fabian, P. Nagler, C. Schüller, T. Korn, P. G. Hawkins, J. T. Steiner, U. Huttner, S. W. Koch, M. Kira, and R. Huber, Lightwave valleytronics in a monolayer of tungsten diselenide, Nature (London) **557**, 76 (2018).

[29] M.-X. Guan, C. Lian, S.-Q. Hu, H. Liu, S.-J. Zhang, J. Zhang, and S. Meng, Cooperative evolution of intraband and interband excitations for high-harmonic generation in strained MoS_2, Phys. Rev. B **99**, 184306 (2019).

[30] N. Klemke, N. Tancogne-Dejean, G. M. Rossi, Y. Yang, F. Scheiba, R. E. Mainz, G. Di Sciacca, A. Rubio, F. X. Kärtner, and O. D. Mücke, Polarization-state-resolved high-harmonic spectroscopy of solids, Nat. Commun. **10**, 1319 (2019).

[31] M. S. Mrudul, A. Pattanayak, M. Ivanov, and G. Dixit, Direct numerical observation of real-space recollision in high-order harmonic generation from solids, Phys. Rev. A **100**, 043420 (2019).

[32] S. Ghimire and D. A. Reis, High-harmonic generation from solids, Nat. Phys. **15**, 10 (2019).

[33] S. Imai, A. Ono, and S. Ishihara, High harmonic generation in a correlated electron system, Phys. Rev. Lett. **124**, 157404 (2020).

[34] M. Borsch, C. P. Schmid, L. Weigl, S. Schlauderer, N. Hofmann, C. Lange, J. T. Steiner, S. W. Koch, R. Huber, and

M. Kira, Super-resolution lightwave tomography of electronic bands in quantum materials, Science **370**, 1204 (2020).
[35] C. P. Schmid, L. Weigl, P Grössing, V. Junk, C. Gorini, S. Schlauderer, S. Ito, M. Meierhofer, N. Hofmann, D. Afanasiev *et al.*, Tunable non-integer high-harmonic generation in a topological insulator, Nature (London) **593**, 385 (2021).
[36] A. Pattanayak, S. Pujari, and G. Dixit, Role of Majorana fermions in high-harmonic generation from Kitaev chain, Sci. Rep. **12**, 1 (2022).
[37] M. Guan, D. Chen, S. Hu, H. Zhao, P. You, and S. Meng, Theoretical insights into ultrafast dynamics in quantum materials, Ultrafast Science **2022**, 9767251 (2022).
[38] C. Qian, C. Yu, S. Jiang, T. Zhang, J. Gao, S. Shi, H. Pi, H. Weng, and R. Lu, Role of shift vector in high-harmonic generation from noncentrosymmetric topological insulators under strong laser fields, Phys. Rev. X **12**, 021030 (2022).
[39] A. Bharti, M. S. Mrudul, and G. Dixit, High-harmonic spectroscopy of light-driven nonlinear anisotropic anomalous Hall effect in a Weyl semimetal, Phys. Rev. B **105**, 155140 (2022).
[40] E. Goulielmakis and T. Brabec, High harmonic generation in condensed matter, Nat. Photonics **16**, 411 (2022).
[41] C. Heide, Y. Kobayashi, A. C. Johnson, F. Liu, T. F. Heinz, D. A. Reis, and S. Ghimire, Probing electron-hole coherence in strongly driven 2D materials using high-harmonic generation, Optica **9**, 512 (2022).
[42] J. Alcalà, U. Bhattacharya, J. Biegert, M. Ciappina, U. Elu, T. Graß, P. T. Grochowski, M. Lewenstein, A. Palau, T. P. Sidiropoulos *et al.*, High-harmonic spectroscopy of quantum phase transitions in a high-tc superconductor, Proc. Natl. Acad. Sci. USA **119**, e2207766119 (2022).
[43] A. J. Uzan-Narovlansky, Á. Jiménez-Galán, G. Orenstein, R. E. F. Silva, T. Arusi-Parpar, S. Shames, B. D. Bruner, B. Yan, O. Smirnova, M. Ivanov *et al.*, Observation of light-driven band structure via multiband high-harmonic spectroscopy, Nat. Photonics **16**, 428 (2022).
[44] Á. Jiménez-Galán, C. Bossaer, G. Ernotte, A. M. Parks, R. E. F. Silva, D. M. Villeneuve, A. Staudte, T. Brabec, A. Luican-Mayer, and G. Vampa, Orbital perspective on high-harmonic generation from solids, Nat. Commun. **14**, 8421 (2023).
[45] O. Neufeld, N. Tancogne-Dejean, H. Hübener, U. De Giovannini, and A. Rubio, Are there universal signatures of topological phases in high-harmonic generation? Probably not, Phys. Rev. X **13**, 031011 (2023).
[46] D. Bauer and K. K. Hansen, High-harmonic generation in solids with and without topological edge states, Phys. Rev. Lett. **120**, 177401 (2018).
[47] H. Liu, Y. Li, Y. S. You, S. Ghimire, T. F. Heinz, and D. A. Reis, High-harmonic generation from an atomically thin semiconductor, Nat. Phys. **13**, 262 (2017).
[48] N. Yoshikawa, T. Tamaya, and K. Tanaka, High-harmonic generation in graphene enhanced by elliptically polarized light excitation, Science **356**, 736 (2017).
[49] M. Taucer, T. J. Hammond, P. B. Corkum, G. Vampa, C. Couture, N. Thiré, B. E. Schmidt, F. Légaré, H. Selvi, N. Unsuree *et al.*, Nonperturbative harmonic generation in graphene from intense midinfrared pulsed light, Phys. Rev. B **96**, 195420 (2017).
[50] N. Tancogne-Dejean and A. Rubio, Atomic-like high-harmonic generation from two-dimensional materials, Sci. Adv. **4**, eaao5207 (2018).
[51] M. S. Mrudul, N. Tancogne-Dejean, A. Rubio, and G. Dixit, High-harmonic generation from spin-polarised defects in solids, npj Comput. Mater. **6**, 10 (2020).
[52] L. Yue and M. B. Gaarde, Imperfect recollisions in high-harmonic generation in solids, Phys. Rev. Lett. **124**, 153204 (2020).
[53] M. S. Mrudul, Á. Jiménez-Galán, M. Ivanov, and G. Dixit, Light-induced valleytronics in pristine graphene, Optica **8**, 422 (2021).
[54] Y. Kobayashi, C. Heide, H. K. Kelardeh, A. Johnson, F. Liu, T. F. Heinz, D. A. Reis, and S. Ghimire, Polarization flipping of even-order harmonics in monolayer transition-metal dichalcogenides, Ultrafast Science **2021**, 9820716 (2021).
[55] N. Rana, M. S. Mrudul, and G. Dixit, Generation of circularly polarized high harmonics with identical helicity in two-dimensional materials, Phys. Rev. Appl. **18**, 064049 (2022).
[56] S. Cha, M. Kim, Y. Kim, S. Choi, S. Kang, H. Kim, S. Yoon, G. Moon, T. Kim, Y. W. Lee *et al.*, Gate-tunable quantum pathways of high harmonic generation in graphene, Nat. Commun. **13**, 6630 (2022).
[57] H. K. Avetissian, S. S. Israelyan, H. H. Matevosyan, and G. F. Mkrtchian, Saddle-point exciton signature on high-order harmonic generation in two-dimensional hexagonal nanostructures, Phys. Rev. A **105**, 063504 (2022).
[58] R. Boyero-García, A. García-Cabrera, O. Zurrón-Cifuentes, C. Hernández-García, and L. Plaja, Non-classical high harmonic generation in graphene driven by linearly-polarized laser pulses, Opt. Express **30**, 15546 (2022).
[59] H. K. Avetissian, G. F. Mkrtchian, K. G. Batrakov, S. A. Maksimenko, and A. Hoffmann, Multiphoton resonant excitations and high-harmonic generation in bilayer graphene, Phys. Rev. B **88**, 165411 (2013).
[60] M. S. Mrudul and G. Dixit, High-harmonic generation from monolayer and bilayer graphene, Phys. Rev. B **103**, 094308 (2021).
[61] Y. Ren, L. Jia, Y. Zhang, Z. Zhang, S. Xue, S. Yue, and H. Du, Orientation dependence of even-order harmonics generation in biased bilayer graphene, Phys. Rev. A **106**, 033123 (2022).
[62] T. N. Ikeda, High-order nonlinear optical response of a twisted bilayer graphene, Phys. Rev. Res. **2**, 032015(R) (2020).
[63] M. Du, C. Liu, Z. Zeng, and R. Li, High-order harmonic generation from twisted bilayer graphene driven by a midinfrared laser field, Phys. Rev. A **104**, 033113 (2021).
[64] E. B. Molinero, A. Datta, M. J. Calderón, E. Bascones, and R. E. F. Silva, High-harmonic generation with a twist: All-optical characterization of magic-angle twisted bilayer graphene, Optica **11**, 171 (2024).
[65] S. Ulstrup, J. C. Johannsen, F. Cilento, J. A. Miwa, A. Crepaldi, M. Zacchigna, C. Cacho, R. Chapman, E. Springate, S. Mammadov *et al.*, Ultrafast dynamics of massive Dirac fermions in bilayer graphene, Phys. Rev. Lett. **112**, 257401 (2014).
[66] G. Le Breton, A. Rubio, and N. Tancogne-Dejean, High-harmonic generation from few-layer hexagonal boron nitride: Evolution from monolayer to bulk response, Phys. Rev. B **98**, 165308 (2018).
[67] F. Hipolito, A. Taghizadeh, and T. G. Pedersen, Nonlinear optical response of doped monolayer and bilayer graphene: Length gauge tight-binding model, Phys. Rev. B **98**, 205420 (2018).

[68] Y. Lee, D. Kim, D.-E. Kim, and A. Chacón, High harmonic generation in monolayer and bilayer of transition metal dichalcogenide, Symmetry **13**, 2403 (2021).

[69] P. Kumar, T. M. Herath, and V. Apalkov, Bilayer graphene in strong ultrafast laser fields, J. Phys.: Condens. Matter **33**, 335305 (2021).

[70] I. Alonso Calafell, L. A. Rozema, A. Trenti, J. Bohn, E. J. C. Dias, P. K. Jenke, K. S. Menghrajani, D. Alcaraz Iranzo, F. J. García de Abajo, F. H. L. Koppens *et al.*, High-harmonic generation enhancement with graphene heterostructures, Adv. Opt. Mater. **10**, 2200715 (2022).

[71] D. Kim, Y. Lee, A. Chacón, and D.-E. Kim, Effect of interlayer coupling and symmetry on high-order harmonic generation from monolayer and bilayer hexagonal boron nitride, Symmetry **14**, 84 (2022).

[72] C. Heide, Y. Kobayashi, A. C. Johnson, T. F. Heinz, D. A. Reis, F. Liu, and S. Ghimire, High-harmonic generation from artificially stacked 2D crystals, Nanophotonics **12**, 255 (2023).

[73] C. Liu, Y. Zheng, Z. Zeng, and R. Li, Driving-laser ellipticity dependence of high-order harmonic generation in graphene, Phys. Rev. A **97**, 063412 (2018).

[74] Y. Feng, S. Shi, J. Li, Y. Ren, X. Zhang, J. Chen, and H. Du, Semiclassical analysis of ellipticity dependence of harmonic yield in graphene, Phys. Rev. A **104**, 043525 (2021).

[75] Ó. Zurrón-Cifuentes, R. Boyero-García, C. Hernández-García, A. Picón, and L. Plaja, Optical anisotropy of non-perturbative high-order harmonic generation in gapless graphene, Opt. Express **27**, 7776 (2019).

[76] E. S. Morell, J. D. Correa, P. Vargas, M. Pacheco, and Z. Barticevic, Flat bands in slightly twisted bilayer graphene: Tight-binding calculations, Phys. Rev. B **82**, 121407(R) (2010).

[77] P. Moon and M. Koshino, Energy spectrum and quantum Hall effect in twisted bilayer graphene, Phys. Rev. B **85**, 195458 (2012).

[78] S. Reich, J. Maultzsch, C. Thomsen, and P. Ordejon, Tight-binding description of graphene, Phys. Rev. B **66**, 035412 (2002).

[79] A. F. Kemper, B. Moritz, J. K. Freericks, and T. P. Devereaux, Theoretical description of high-order harmonic generation in solids, New J. Phys. **15**, 023003 (2013).

[80] M. Lewenstein, P. Balcou, M Yu Ivanov, A. L'huillier, and P. B. Corkum, Theory of high-harmonic generation by low-frequency laser fields, Phys. Rev. A **49**, 2117 (1994).

[81] P. Dietrich, N. H. Burnett, M. Ivanov, and P. B. Corkum, High-harmonic generation and correlated two-electron multiphoton ionization with elliptically polarized light, Phys. Rev. A **50**, R3585 (1994).

[82] F. Sekiguchi, M. Sakamoto, K. Nakagawa, H. Tahara, S. A. Sato, H. Hirori, and Y. Kanemitsu, Enhancing high harmonic generation in GaAs by elliptically polarized light excitation, Phys. Rev. B **108**, 205201 (2023).

[83] A. C. Ferrari and D. M. Basko, Raman spectroscopy as a versatile tool for studying the properties of graphene, Nat. Nanotechnol. **8**, 235 (2013).

[84] C. H. Lui, Z. Li, Z. Chen, P. V. Klimov, L. E. Brus, and T. F. Heinz, Imaging stacking order in few-layer graphene, Nano Lett. **11**, 164 (2011).

[85] C. H. Lui, L. M. Malard, SukHyun Kim, G. Lantz, F. E Laverge, R. Saito, and T. F Heinz, Observation of layer-breathing mode vibrations in few-layer graphene through combination Raman scattering, Nano Lett. **12**, 5539 (2012).

[86] N. Rana, M. S. Mrudul, D. Kartashov, M. Ivanov, and G. Dixit, High-harmonic spectroscopy of coherent lattice dynamics in graphene, Phys. Rev. B **106**, 064303 (2022).

[87] O. Neufeld, J. Zhang, U. De Giovannini, H. Hübener, and A. Rubio, Probing phonon dynamics with multidimensional high harmonic carrier-envelope-phase spectroscopy, Proc. Natl. Acad. Sci. USA **119**, e2204219119 (2022).

[88] N. Rana and G. Dixit, Probing phonon-driven symmetry alterations in graphene via high-order-harmonic spectroscopy, Phys. Rev. A **106**, 053116 (2022).